Journal of the Mechanics and Physics of Solids 142 (2020) 104041

Contents lists available at ScienceDirect

Journal of the Mechanics and Physics of Solids

journal homepage: www.elsevier.com/locate/jmps

Modeling the mechanics, kinetics, and network evolution of photopolymerized hydrogels

Hongyuan Zhu[a,b], Xiaoxiao Yang[a,b], Guy M. Genin[a,b,c,d], Tian Jian Lu[e,f], Feng Xu[a,b], Min Lin[a,b,*]

[a] The Key Laboratory of Biomedical Information Engineering of Ministry of Education, School of Life Science and Technology, Xi'an Jiaotong University, Xi'an 710049, PR China
[b] Bioinspired Engineering & Biomechanics Center (BEBC), Xi'an Jiaotong University, Xi'an 710049, PR China
[c] Department of Mechanical Engineering & Materials Science, Washington University in St. Louis, St. Louis 63130, MO, USA
[d] NSF Science and Technology Center for Engineering Mechanobiology, Washington University in St. Louis, St. Louis 63130, MO, USA
[e] State Key Laboratory of Mechanics and Control of Mechanical Structures, Nanjing University of Aeronautics and Astronautics, Nanjing 210016, PR China
[f] MOE Key Laboratory for Multifunctional Materials and Structures, Xi'an Jiaotong University, Xi'an 710049, PR China

ARTICLE INFO

Article history:
Received 6 January 2020
Revised 5 May 2020
Accepted 25 May 2020
Available online 2 June 2020

Keywords:
Photopolymerized hydrogel
Mechanical properties
Photobleaching
Loop formation
Frontal photopolymerization

ABSTRACT

Photopolymerized hydrogels are critical to soft devices, mechanobiology, regenerative medicine, and next generation drug delivery. However, the optimization of processing protocols for all of these applications of photopolymerized hydrogels has been at least semi-empirical due to the lack of a comprehensive predictive framework. Herein, we developed the first comprehensive predictive framework for how the chemical kinetics, optical properties, and mechanical properties of a photopolymerized hydrogel emerge from a precursor solution as the solution is illuminated, and of how these processing parameters relate to the final mechanics of the hydrogel. We validated the model experimentally using an eosin Y-initiated di-acrylate system. The model revealed that processing kinetics were dominated by photobleaching and crosslinking, and that network mechanics were dominated by chain growth and loop formation. We demonstrated the utility of the model by using it to design and then synthesize hydrogels with specified gradients in mechanical properties. The modeling framework is general and enables design of a broad range of hydrogels.

1. Introduction

Photo-initiated hydrogels are key technologies for cell culture, regenerative medicine, drug delivery, and soft devices (Brown and Anseth, 2017; Layani et al., 2018; Ruskowitz and DeForest, 2018; Wang et al., 2016a; Yao et al., 2018; Yuk et al., 2019). Development of these materials is typically empirical, with little guidance from theoretical models. Although many outstanding constitutive models exist for hydrogels and polymers, an unmet need is to predict how processing conditions, such as precursor chemical concentrations and illumination, can be varied to produce hydrogels with specific mechanical properties (Feng et al., 2016; Gao et al., 2016). This is a limitation for the entire range of synthesis methods, including light-triggered bond exchange reactions (Long et al., 2009; Ma et al., 2014; Zou et al., 2017), light-induced liquid crystal deformation (Krishnan and Johnson, 2014), light-induced shape memory (Lendlein et al., 2005), photo-induced plasticity, photodegradation, photoisomerization, and photopolymerization (Wu et al., 2018). We therefore developed a predictive

* Corresponding author.
E-mail address: minlin@mail.xjtu.edu.cn (M. Lin).

https://doi.org/10.1016/j.jmps.2020.104041
0022-5096/

framework for how the chemical kinetics, optical properties, and mechanical properties of a photopolymerized hydrogel emerge from a precursor solution, and validated it on a technologically important hydrogel system.

In photopolymerized hydrogels, a photo-initiator is progressively consumed in response to illumination, changing the optical properties, crosslinking kinetics, and ultimately mechanical properties of the hydrogel (Corrigan et al., 2018). Our framework began with a model of photo-initiator kinetics. Photo-initiators come in two classes according to their photochemical products: type I, which generate initiating radicals via light induced bond cleavage, and type II, which generate radicals when a light-excited photo-initiator interacts with co-initiators via hydrogen abstraction, electron transfer, oxidation, and reduction (Dadashi-Silab et al., 2016). Our focus was type II photo-initiators, in which the excited initiator either returns its ground state reversibly or photobleaches irreversibly, generating a leuco-product (Gorner, 2008; Herculano et al., 2013; Zhu et al., 2018). Photobleaching decreases initiation efficiency and reduces the absorption of the precursor solution. The first component of our framework was therefore developing a model of how photo-initiator consumption affects photopolymerization reaction kinetics. We focused initially on an eosin Y/amine hydrogel system because certain baseline measurements of photobleaching kinetics are already available in the literature (Zhu et al., 2018).

The second component of the framework was modeling how network mechanics emerge over time. As polymer emerges, loops and crosslinks form that determine the emergence of mechanical properties (Lin et al., 2018; Wang et al., 2016b; Zhong et al., 2016). Existing models predict that the elastic modulus of a hydrogel rises in proportional to crosslink density (Nishi et al., 2017), so elastic modulus increases linearly with polymer concentration if all possible crosslinking sites on each polymer strand are crosslinked. However, this trend does not capture the response of polymer solutions with concentrations sufficiently low that a substantial fraction of polymer strands crosslink with themselves, creating loop defects instead of efficient crosslinks. These loops decrease the crosslinking density, and thus interfere with branch-like structures, delay gelation, and weaken the hydrogel (Zhong et al., 2016). Although loop formation and its effect on mechanics are well understood in step growth hydrogels (Lin et al., 2018; Wang et al., 2016b; 2017a; Wang et al., 2017b, 2016c; Zhong et al., 2016; Zhou et al., 2012), no previous model exists for photo-initiated hydrogels.

The third component of the framework was modeling how "frontal photopolymerization" (FPP) affects kinetics. FPP occurs in optically thick samples, in which photopolymerization forms a propagating wave of network solidification (Cabral and Douglas, 2005; Cabral et al., 2004). Coarse-grained kinetic models exist for how FPP affects optical properties (Cabral et al., 2004; Hennessy et al., 2015b; Vitale and Cabral, 2016; Warren et al., 2005), mass diffusion (Hennessy et al., 2015b, 2017), heating (Hennessy et al., 2015a) (Hennessy et al., 2017; Vitale et al., 2015a, b), thermal diffusion (Hennessy et al., 2015a), and polymer kintics (Vitale et al., 2015b). However, the key parameters that feed into the other models in our framework, specifically associated with the physics underlying the spatiotemporal polymer conversion fraction and the absorption coefficient, are not available in this coarse-grained approach. We therefore undertook a detailed analysis of molecular changes in FPP.

We integrated these components into a comprehensive framework for predicting and designing formation-structure-property relationships in type II photo-initiated photopolymerization. We used eosin Y-initiated polyethylene glycol diacrylate (PEGDA) hydrogels as an example. We established a theoretical model combining photopolymerization kinetics and hydrogel mechanics for predicting the spatiotemporal evolution of concentrations of chemical species, gel points and mechanical properties of hydrogel under various precursor compositions, light irradiation doses and sample thicknesses. To verify the model, we experimentally measured the photo-initiator conversion kinetics, the evolution of carbon double bonds, the conditions for gelation, and the shear moduli in cured hydrogels using UV–vis spectra, FTIR, rheology, and indentation experiments. Finally, we applied the validated model to successfully design the specific depth-dependent frontal photopolymerization processes and define interfacial profiles of eosin Y and acrylate.

2. Theory

The model predicted how the evolution of eosin Y (EY) consumption and acrylate (CC) on PEGDA combined to predict the evolution of hydrogel properties as a light source of intensity I_0 and frequency ν_0 irradiated the hydrogel surface (Fig. 1). For each component α (α = EY, CC, or PEGDA), the fractional concentration $X_\alpha(t)$ and fractional conversion $P_\alpha(t)$ at time t were calculated as:

$$\begin{cases} X_\alpha(t) = \frac{[\alpha]}{[\alpha]_0} \\ P_\alpha(t) = 1 - X_\alpha(t) = 1 - \frac{[\alpha]}{[\alpha]_0} \end{cases} \tag{1}$$

here $[\alpha]_0$ and $[\alpha]$ are the initial molar concentration and molar concentration at time t of phase α, respectively. $[\mathrm{PEGDA}]_0$ denotes the initial concentration of PEGDA where its unit "%" represents its weight percentage in the hydrogel precursor. Pure PEGDA ($M_W \approx 575$ g mol^{-1}, $[\mathrm{PEGDA}]_0 = 100\%$) at room temperature contains approximately 3.48 M^{-1} acrylates; there are $f = 2$ functional groups on a single PEGDA molecule.

2.1. Component 1: kinetics of photobleaching dependent photopolymerization

2.1.1. Photobleaching

An initiation mechanism similar to that of as eosin Y/thiol has been proposed for the eosin Y/amine initiation system (Zhu et al., 2018). The consumption of eosin Y can be described by

$$X_{\mathrm{EY}} = \exp\left(-k_{\mathrm{pb}} t\right) \tag{2}$$

where k_{pb} denotes the kinetic constant of photobleaching.

The consumption of eosin Y can be further described by the following sub-processes (Zhu et al., 2018): (**Process 1**) an eosin Y molecule in the ground state (EY) is excited to the triplet state (EY^{3*}) by irradiation. (**Process 2**) EY^{3*} is subsequently quenched by oxygen or emits phosphorescence, or (**Process 3**) turns into the reductive radical form ($EY^{\bullet -}$) through reaction with an amine and other organic compounds. (**Process 4**) $EY^{\bullet -}$ is then quenched by oxygen, or (**Process 5**) changes into the leuco-product (EYH_2). Let k_i (i = 1–5) represent the kinetic constant of **Process *i***; then, these processes can be described by a set of kinetic equations as follows:

$$\frac{d[EY_0]}{dt} = -k_1[EY] + k_2\left[EY^{3*}\right] + k_2\left[EY^{\cdot -}\right] \tag{3}$$

$$\frac{d\left[EY^{3*}\right]}{dt} = -(k_2 + k_3)\left[EY^{3*}\right] + k_1[EY_0] \tag{4}$$

$$\frac{d[EY^{\cdot -}]}{dt} = -(k_4 + k_5)\left[EY^{\cdot -}\right] + k_3\left[EY^{3*}\right] \tag{5}$$

$$\frac{d[EYH_2]}{dt} = k_5\left[EY^{\cdot -}\right] \tag{6}$$

$$[EY_0] + \left[EY^{3*}\right] + \left[EY^{\cdot -}\right] + [EYH_2] = 1 \tag{7}$$

where $k_1 = \sigma I_0/h\nu_0$ and $k_3 = k_{et}\bullet[TEOA]_0$, in which σ is the absorption cross-section of ground-state eosin Y, h is Planck's constant, and k_{et} is the reductive electron transfer rate constant from triplet eosin Y to TEOA.

According to Eqs. (3)–(7), the relationships between kpb, the initial co-initiator concentration ($[TEOA]_0$), and the surface light intensity (I_0) can be described by (Zhu et al., 2018):

$$k_{pb} = \frac{k_{et0} + k_{et}\cdot[TEOA]_0}{k_2 + k_{et0} + k_{et}\cdot[TEOA]_0}\frac{k_5}{k_4 + k_5}\frac{\sigma I_{ex}}{h\upsilon} \tag{8}$$

2.1.2. Photopolymerization

The eosin Y/amine initiated photopolymerization of PEGDA can be described by the following equations according to reactions listed in Table A1:

$$\frac{d[TEOA^{\cdot}]}{dt} = R_i - k_i[TEOA^{\cdot}][CC] \tag{9}$$

$$\frac{d[CC]}{dt} = -k_i[TEOA^{\cdot}][CC] - k_p[CC^{\cdot}][CC] \tag{10}$$

$$\frac{d[TEOA]}{dt} = [TEOA] - [TEOA^{\cdot}] \tag{11}$$

$$\frac{d[CC^{\cdot}]}{dt} = k_i[TEOA^{\cdot}][CC] - 2k_t[CC^{\cdot}][CC^{\cdot}] \tag{12}$$

where R_i is the initiation rate (amount of TEOA radical generated per unit of time) and k_i, k_p, and k_t are kinetic constants for initiation, propagation, and termination, respectively.

These kinetic equations can be simplified to obtain an explicit expression of P_{CC}. Because $[TEOA^{\bullet}] << [TEOA]$, and considering the non-consumption of TEOA, ($d[TEOA^{\bullet}]/dt \approx 0$), from Eq. (9):

$$R_i = k_i[TEOA^{\cdot}][CC] \tag{13}$$

Considering that the radical propagation can reach a quasi-equilibrium state in the reaction ($d[CC^{\bullet}]/dt \approx 0$), from Eq. (12):

$$[CC^{\cdot}] = \sqrt{\frac{k_i[TEOA^{\cdot}][CC]}{2k_t}} \tag{14}$$

Using Eqs. (13) and (14):

$$[CC^{\cdot}] = \sqrt{R_i/2k_t} \tag{15}$$

Through Eqs. (10) and (15), the following can be obtained:

$$\frac{d[CC]}{dt} = -R_i - k_p\sqrt{\frac{R_i}{2k_t}}[CC] = -R_i - R_p \tag{16}$$

where R_p is the radical propagation rate. Generally, $R_i << R_p$ holds true for most of the previous photopolymerization studies (Cramer et al., 2003; Lee et al., 2014). Thus omitting Ri in Eq. (16), the following can be obtained:

$$\frac{dX_{CC}}{dt} = -k_p\sqrt{\frac{R_i}{2k_t}}X_{CC} \tag{17}$$

It has been demonstrated that R_i is dependent on $[EY]_t$, $[TEOA]_t$, and I_0 (Lee et al., 2014):

$$R_i = \gamma[EY][TEOA]I_0 \tag{18}$$

For a homogeneous system, only $[EY]_t$ is considered to vary with time and $R_i = R_{i0}\bullet\exp(-k_{pb}\bullet t)$, where R_{i0} is the initial value of R_i and is dependent on the initial chemical composition and light intensity (*i.e.* $[PEGDA]_0$, $[TEOA]_0$, $[EY]_0$, I_0). Thus, by integrating both sides of Eq. (17), the kinetic process of eosin Y-initiated photopolymerization in a homogeneous reaction system can be approximated as follows:

$$X_{CC} = \exp\left(-b + b\exp\left(-k_{pb}t/2\right)\right) \tag{19}$$

where $b = \frac{k_p}{k_{pb}}\sqrt{2R_{i0}/k_t}$. This equation was used to fit the experimental data of the time dependent fractional concentration of acrylate.

2.2. Component 2: the emergence of mechanical properties

A modified Macosko model (Macosko and Miller, 1976; Miller and Macosko, 1976) was used to determine the densities of the efficient elastic chains and loops in PEGDA hydrogels, which were subsequently used to predict PEGDA hydrogel elasticity. Because the rate of radical propagation is far greater than that of radical termination ($R_p >> R_t$) in most free radical polymerizations, the effect of radical termination on the network topology was not considered. Instead, the propagation process was divided into two parts, *i.e.* intermolecular reactions for crosslink formation and intramolecular reactions for loop formation. The rates of intramolecular (R_{pl}) and intermolecular (R_{pc}) propagation depend on the internal (C_{int}) and external (C_{ext}) concentrations of the functional groups as follows:

$$\frac{R_{pl}}{R_{pc}} = \frac{C_{int}}{C_{ext}} \tag{20}$$

C_{int} depends on the molecular properties of the polymer, but not on initial polymer concentration (*i.e.* $[PEGDA]_0$), whereas C_{ext} is proportional to the initial polymer concentration (Dutton et al., 1996; Rolfes and Stepto, 1990). To simplify the calculation, the loop formation probability was considered to be constant over the entire duration of photopolymerization. Thus, $R_{pl}/R_{pc}=2C_0/[PEGDA]_0$, where C_0 is a constant and denotes the critical concentration of $[PEGDA]_0$ below which the precursor cannot be crosslinked even as acrylates are fully consumed.

The probability θ that an acrylate molecule will react through intermolecular propagation is as follows:

$$\theta = \frac{R_{pc}}{R_{pc}+R_{pl}} = \frac{[PEGDA]_0}{[PEGDA]_0 + 2C_0} \tag{21}$$

(1) Pre-gelation

The gel point of the hydrogel is the time when an effectively "infinite" molecule emerges, and could be estimated by the average molecular weight (Flory, 1941; Macosko and Miller, 1976; Wang et al., 2017b). W^{out}_{CC*} is defined as the expected molecular weight attached to the carbon end when looking out from a random carbon double bond. WCC*out is the expected molecular weight attached to the carbon end when looking out from a random carbon radical and the average values of these two weights can be described as follows:

$$E\left(W^{out}_{CC}\right) = P_{CC}E\left(W^{out}_{CC*}\right) + (1-P_{CC})0 \tag{22}$$

If a acrylate reacts intramolecularly, $E(W^{out}_{CC*}) = 0$; if a acrylate reacts intermolecularly, $E(W^{out}_{CC*})$ equals the expected weight $E(W^{in}_{CC*})$ attached to carbon end when looking inwards from a random carbon double bond:

$$E\left(W^{out}_{CC*}\right) = \theta E\left(W^{in}_{CC*}\right) + (1-\theta)0 = \theta E\left(W^{in}_{CC*}\right) \tag{23}$$

As PEGDA is a di-functional polymer strand, W^{in}_{CC*}, the weight attached to the carbon end when looking inward from a random carbon radical, is composed of three parts: the weight of the PEGDA itself, the weight attached to the reacted carbon radical, and the weight attached to the remaining carbon double bond; thus,

$$E\left(W^{in}_{CC*}\right) = M_{PEGDA} + E\left(W^{out}_{CC*}\right) + 2E\left(W^{out}_{CC}\right) \tag{24}$$

From Eqs. (22)–(24),

$$E\left(W^{out}_{CC*}\right) = \frac{\theta M_{PEGDA}}{1-\theta(1+2P_{CC})} \tag{25}$$

The gelation point, which is the diverged point of average molecular weight, can be described as follows:

$$P_{\text{gel}} = \frac{1-\theta}{2\theta} \tag{26}$$

If $P_{\text{gel}} \geq 1$, the precursor cannot be cured even if all PEGDA has reacted. Thus, from Eqs. (21) and (26), when $[\text{PEGDA}]_0 \leq C_0$, the precursor is not crosslinked despite the full conversion of acrylates. To obtain an ideal network without loops, $\theta \to 1$, $P_{\text{gel}} \to 0$, indicating crosslinking at an extremely low conversion.

(2) Post-gelation

After gelation, the crosslink density can be calculated by counting the "infinite" ends on each PEGDA strand. We denote $F_{\text{CC}}^{\text{out}}$ as an event where a carbon end links to a finite chain when looking out from a random carbon double bond, the probability of which is $\phi(F_{\text{CC}}^{\text{out}})$, and $F_{\text{CC}*}^{\text{out}}$ as an event where a carbon end on a reacted acrylate links to a finite chain when looking out from a random carbon radical, the probability of which is $\phi(F_{\text{CC}*}^{\text{out}})$, we can write the following:

$$\phi\left(F_{\text{CC}}^{\text{out}}\right) = P_{\text{CC}}\phi\left(F_{\text{CC}*}^{\text{out}}\right) + (1 - P_{\text{CC}}) \tag{27}$$

If a carbon end links to a chain via intramolecular reaction $\phi(F_{\text{CC}*}^{\text{out}}) = 1$; if it links to chains via intermolecular reaction $\phi(F_{\text{CC}*}^{\text{out}}) = \phi(F_{\text{CC}*}^{\text{in}})$, in which $\phi(F_{\text{CC}*}^{\text{in}})$denotes probability of linking to a finite chain when looking into a random carbon radical. Thus,

$$\phi\left(F_{\text{CC}*}^{\text{out}}\right) = \theta\phi\left(F_{\text{CC}*}^{\text{in}}\right) + (1 - \theta) \tag{28}$$

in which

$$\phi\left(F_{\text{CC}*}^{\text{in}}\right) = \phi\left(F_{\text{CC}*}^{\text{out}}\right)\phi(E_{\text{CC}}) \tag{29}$$

where E_{CC} is an event in which neither of the remaining 2 arms extends to infinity. $\phi(E_{\text{CC}})$ can be calculated using the following equation (Miller and Macosko, 1976; Reddy et al., 2006):

$$\phi(E_{\text{CC}}) = P_{\text{CC}}\phi\left(F_{\text{CC}}^{\text{out}}\right) + 1 - P_{\text{CC}} \tag{30}$$

From Eqs. (28)–(30),

$$\phi\left(F_{\text{CC}*}^{\text{out}}\right) = \frac{1-\theta}{1-\theta\phi(E_{\text{CC}})} \tag{31}$$

Combining Eqs. (30) and (31), the solution of $\phi(F_{\text{CC}*}^{\text{out}})$ can be obtained.

The probability of k acrylates ($k \in \{0, 1, 2\}$) reacting on a PEGDA molecule is given as follows:

$$\phi(k \text{ reacted acrylates}) = \binom{f}{k} P_{\text{CC}}^{k}(1 - P_{\text{CC}})^{f-k} \tag{32}$$

If k ($k \in \{1, 2\}$) acrylates reacted, m ($m \in \{0, 1, 2, 3, 4\}$) carbons attach to an infinite network:

$$\phi(m \text{ infinite ends}|k \text{ reacted acrylates}) = \binom{2k}{m}\phi\left(F_{\text{CC}*}^{\text{out}}\right)^{2k-m}\left(1 - \phi\left(F_{\text{CC}*}^{\text{out}}\right)\right)^{m} \tag{33}$$

Thus, the probability of a PEGDA molecule contains m end to infinity is:

$$\phi(\chi_m) = \sum_{k} \phi(m \text{ infinite ends}|k \text{ reacted acrylates})\phi(k \text{ reacted acrylates}) \tag{34}$$

Thus, the fractional crosslinking density (η) of the PEGDA network can be calculated as:

$$\eta = \sum_{m=3}^{2f} \frac{m-2}{2}\phi(\chi_m) \tag{35}$$

For a network without loop formation, $q = 1$, $\phi(F_{\text{CC}*}^{out}) = 0$, and:

$$\eta = \phi(k \text{ reacted acrylates})|_{k=2} = P_{\text{CC}}^{2} \tag{36}$$

A loop can be defined as the chain formed by the intramolecular reaction of two carbon ends. Thus, the total density of loops (l) is the number of chains formed by reacting acrylate with a finite path as follows:

$$l = \phi\left(F_{\text{CC}*}^{\text{out}}\right)P_{\text{CC}}\upsilon_0 \tag{37}$$

where ν_0 is the density of the efficient elastic chains of an ideal network (no loop formation). Because each ideal crosslinked PEGDA strand contains 4 carbon ends on efficient elastic chains and each chain is formed by 2 ends, it can be calculated as $\nu_0 = 2N_{\text{A}}[\text{PEGDA}]_0$, where N_{A} is Avogadro's constant.

It should be noted that this model can only provide the total density of loops but cannot distinguish loop order (the number of polymer strands between the carbon ends before linking (Wang et al., 2016b)). Thus, only the mechanical contribution of the crosslink density is considered and the shear modulus was estimated by phantom theory as follows (Nishi et al., 2017):

$$G = \eta N_A [\mathrm{PEGDA}]_0 kT = \frac{1}{2}\eta \upsilon_0 k_B T \tag{38}$$

where k is Boltzmann's constant and T is the absolute temperature. Here, we presume that the shear modulus of the fully cured sample (when acrylate is consumed) is G_{final}, and the ideal network without loop formation is $G_{\mathrm{ideal}} = 1/2 \cdot \nu_0 kT$. Thus, the fractional crosslinking density (η) is equal to the ratio between the shear modulus of cured sample and the ideal shear modulus (G/G_{ideal}).

2.3. Component 3: frontal photopolymerization

The frontal photopolymerization (FPP) process in an optically thick sample was considered next. The absorption coefficient can be calculated by the sum of the absorption coefficients of eosin Y (μ_{EY}) and PEGDA hydrogel (μ_{Const}):

$$\mu = \mu_{\mathrm{EY}} + \mu_{\mathrm{const}} \tag{39}$$

where μ_{EY} is proportional to the remaining concentration of eosin Y,

$$\mu_{\mathrm{EY}} = \varepsilon_{\mathrm{EY}} [\mathrm{EY}]_0 X_{\mathrm{EY}} \tag{40}$$

In which $\varepsilon_{\mathrm{EY}}$ is the molar absorption coefficient of eosin Y.

The light intensity is I, the initial value of μ is μ_0, the normalized absorption coefficient is $\hat{\mu} = \mu/\mu_0$, and the normalized light intensity is $\hat{I} = I/I_0$.

From Eqs. (2) and (8),

$$\frac{dX_{\mathrm{EY}}(z,t)}{dt} = -k_{\mathrm{pb}}(z,t) X_{\mathrm{EY}}(z,t) = -k_{\mathrm{pb0}} \hat{I}(z,t) X_{\mathrm{EY}}(z,t) \tag{41}$$

According to Eqs. (40) and (41),

$$\frac{d\hat{\mu}(z,t)}{dt} = \frac{\mu_{\mathrm{EY}}}{\mu_0}\frac{dX_{\mathrm{EY}}}{dt} = -\frac{\mu_{\mathrm{EY}}[\mathrm{EY}]_0}{\mu_0} k_{\mathrm{pb0}} \hat{I}(z,t) X_{\mathrm{EY}}(z,t) \tag{42}$$

According to the Beer-Lambert law,

$$\frac{d\hat{I}(z,t)}{dt} = -\mu_0 \hat{\mu}(z,t) \hat{I}(z,t) \tag{43}$$

From Eq. (18), the initiation rate at depth z can be described as follows:

$$R_i(z,t) = -R_{i0} X_{\mathrm{EY}}(z,t) \hat{I}(z,t) \tag{44}$$

From Eq. (17), the spatiotemporally dependent fractional concentration of the acrylates can be calculated by:

$$\frac{dX_{\mathrm{CC}}(z,t)}{dt} = -k_p \sqrt{\frac{R_i(z,t)}{2k_t}} X_{\mathrm{CC}}(z,t) \tag{45}$$

Eqs. (41)–(45) were used to simulate the conversion of eosin Y and acrylates in FPP.

The calculated X_{CC} was used to determine the position of the interface between the fully cured and uncured samples, and the stiffness gradient at the interface. Considering a similar interface and gradient of X_{EY} can form in the depth direction, the interfacial position was defined as z_0 (Warren et al., 2005):

$$\left.\frac{d^2 P_x}{dz^2}\right|_{z_0} = 0 (x = \mathrm{EY}, \mathrm{CC}) \tag{46}$$

where dP_α/dz approaches a maximum. The beginning and end of the interface were defined as z_1, z_2 ($z_1 > z_2$), where $dP_\alpha/dz = -\max(-dP_\alpha/dz)/2$. Thus, these positions were defined as z_{EY0}, z_{EY1}, z_{EY2} on the eosin Y conversion profile and as z_{CC0}, z_{CC1}, z_{CC2} on the acrylate conversion profile, respectively. $P_{\mathrm{EY}i}$ ($i = 0, 1, 2$) is the degree of conversion (DoC) of eosin Y at position $z_{\mathrm{EY}i}$, while $P_{\mathrm{CC}i}$ ($i = 0, 1, 2$) is the DoC of acrylate at position $z_{\mathrm{CC}i}$. The width of the interfacial profile was defined as follows:

$$w = z_1 - z_2 \tag{47}$$

All fitting and simulation processes were accomplished in the MATLAB environment (The Mathworks, Natick, MA, USA).The values of all the parameters used in the model could be found in Table A2.

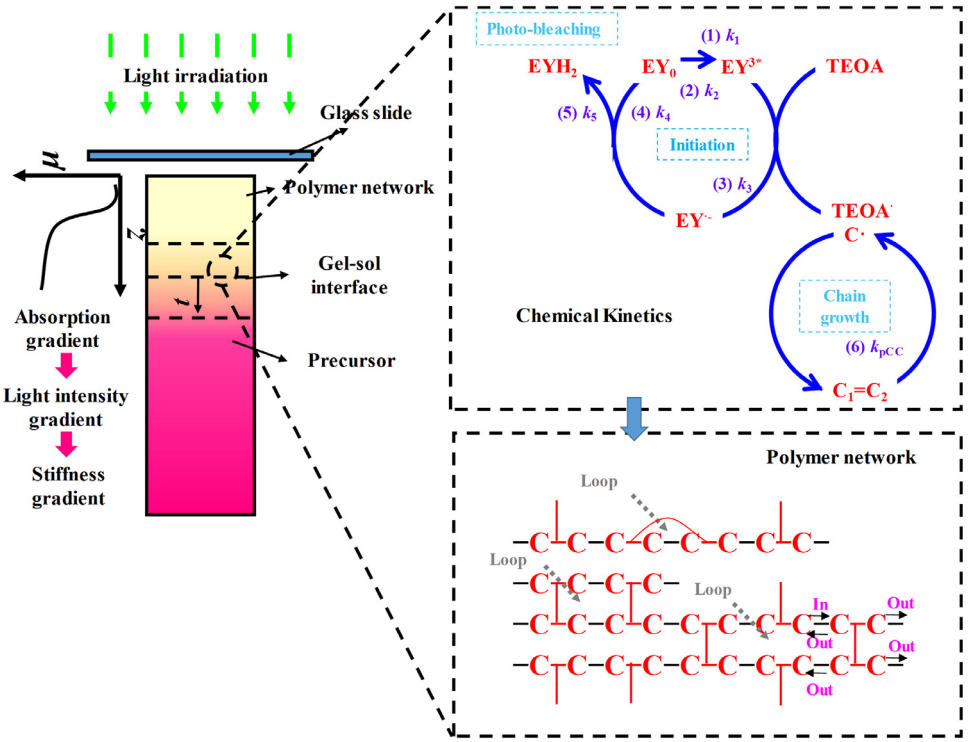

Fig. 1. Schematic of eosin Y/TEOA-initiated photopolymerization of PEGDA. During irradiation of the photocurable sample, the absorption, light intensity, chemical conversion, and elasticity all changed spatiotemporally. Photobleaching of eosin Y changed the absorption gradient and light intensity in the reaction system, which influenced the conversion kinetics of PEGDA. The chemical kinetics determined the formation of polymer networks and the final elasticity gradient in the hydrogels.

3. Experiments and results

3.1. Materials

Polyethylene glycol di-acrylate (PEGDA, $M_W \approx 575$ g mol^{-1}), triethanolamine (TEOA), eosin Y disodium salt, and phosphates were purchased from Sigma-Aldrich (St. Louis, MO, USA). All samples were irradiated using a light-emitting diode (LED) with emission centered at 530 nm. The final concentration of phosphate was brought to 0.01 mM for each sample to adjust the pH to 7.4. The light intensity of the LED was calibrated using an optical meter (Thorlabs PM100D, Newton, NJ, USA). The following tests were performed under atmospheric conditions at room temperature (approximately 300 K).

3.2. UV–vis spectroscopy

To determine the DoC of eosin Y (P_{EY}), the polymer precursors were added to 96-well plates (30 μL in each well) and irradiated using the LED at a defined power for various durations. The UV–vis absorption spectra (400–600 nm) of the curing samples were recorded *in-situ* using a Spark Multimode Microplate Reader (Tecan Group Ltd., Männedorf, Zürich, Switzerland) at room temperature. The DoC of eosin Y was calculated by normalizing the absorbance at 520 nm measured at different times using the following equation:

$$P_{EY} = 1 - \frac{A_{520nm} - (A_{400nm} + A_{600nm})/2}{[A_{520nm} - (A_{400nm} + A_{600nm})/2]_{t=0}} \tag{48}$$

The measurement scheme and representative UV–vis absorption spectra at different irradiation times are shown in Fig. 2. Although the measurements obtained using the Spark Multimode Microplate Reader provided relative absorbance changes during a single curing process, the sample thickness was difficult to estimate due to the concave liquid surface in the well. Therefore, to obtain the thickness-dependent optical properties of the hydrogels, precursors with different initial eosin Y concentrations were added to the cuvette with a thickness of 1 mm and their UV-spectra were measured with a Lambda 35 UV–vis spectrophotometer (Perkin Elmer, USA) (Fig. B1a). The relationship between absorbance and initial eosin Y concentration is shown Fig. B1b. The relationship is linear as described by the Beer-Lambert law, and through linear fitting, the molar absorption coefficient of eosin Y at 515 nm (peak value) was determined to be approximately 0.009 μM^{-1} mm^{-1}, similar to the previously reported value (Shih and Lin, 2013). The constant absorption coefficient of PEGDA hydrogels at 515 nm was approximately 0.2 mm^{-1}.

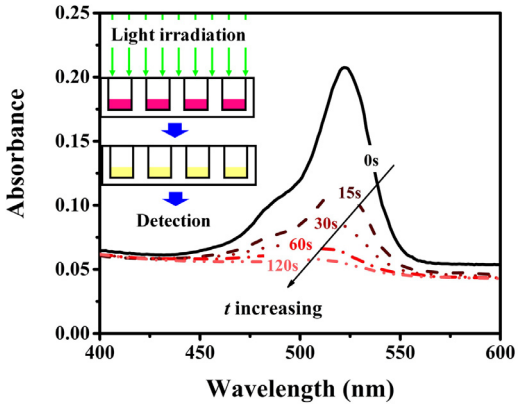

Fig. 2. Schematic of UV–vis absorption measurements and representative data for hydrogels irradiated for prescribed time intervals. As irradiation time increases, the absorption peak of eosin Y at 520 nm decreases gradually, as represented by the fading and differently dashed line styles. These measurements quantified relative changes in the absorbance of multiple reaction samples in a single well plate. For this figure, the initial conditions for the sample were $[EY]_0 = 10\ \mu M$, $[TEOA]_0 = 100$ mM, and $[PEGDA]_0 = 20\%$. The illumination intensity was $I_0 = 50$ mW cm^{-2}.

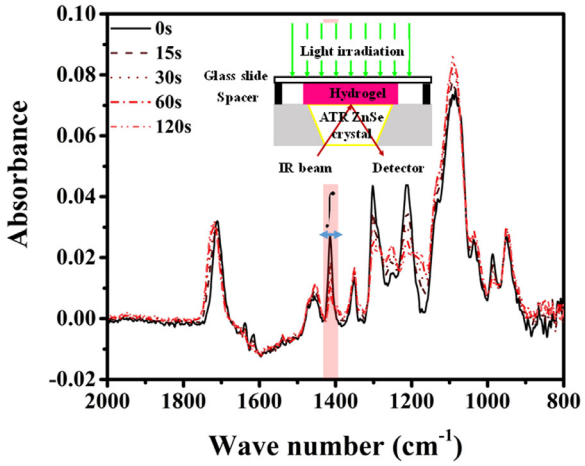

Fig. 3. Schematic of FTIR spectral measurements and representative data for hydrogels irradiated for prescribed time intervals. IR absorbance at the peaks with wave numbers of 1415, 1297, 1254, 1211, 985 cm^{-1} is related to molecular vibration of chemical bonds on acrylates. IR absorbance at these peaks decreased with increasing irradiation time, as represented by the fading and differently dashed line styles. For validation of numerical models, the decay of the peak area around 1415 cm^{-1} was used to estimate the concentration of acrylates. For this figure, the initial conditions for the sample were $[EY]_0 = 10\ \mu M$, $[TEOA]_0 = 100$ mM, and $[PEGDA]_0 = 20\%$. The illumination intensity was $I_0 = 50$ mW cm^{-2}.

3.3. IR spectroscopy

DoC of acrylates (P_{CC}) was measured via Fourier-transform infrared (FTIR) spectra (Nicolet iS 50, Thermo Fisher Scientific, Waltham, MA, USA) equipped with an attenuated total reflection (ATR) accessory. The hydrogel precursors were dropped onto a zinc selenide crystal and covered by a glass slide, while spacers with defined thicknesses were placed between them. The LED was placed on the samples and irradiation was performed for different durations. Each sample was scanned 16 times at a 4 cm^{-1} resolution and averaged results were obtained. The absorbance of distilled water was used as a baseline signal and deducted for each test. The integrated absorbance at approximately 1415 cm^{-1} was used to calculate the fractional concentration of acrylates, as it arises from the deformation of $=CH_2$ (Boonen et al., 2017). The integrated absorbance at approximately 1085 cm^{-1} was used as an internal standard for conversion analysis of each sample, as it corresponds to C–O–C stretching (Boonen et al., 2017). Thus, the DoC of acrylate was determined as follows:

$$P_{CC} = 1 - \frac{A_{1415\text{cm}^{-1}}/A_{1085\text{cm}^{-1}}}{(A_{1415\text{cm}^{-1}}/A_{1085\text{cm}^{-1}})_{t=0}} \tag{49}$$

The measurement scheme and representative FTIR spectra of a sample at different irradiation times is shown in Fig. 3.

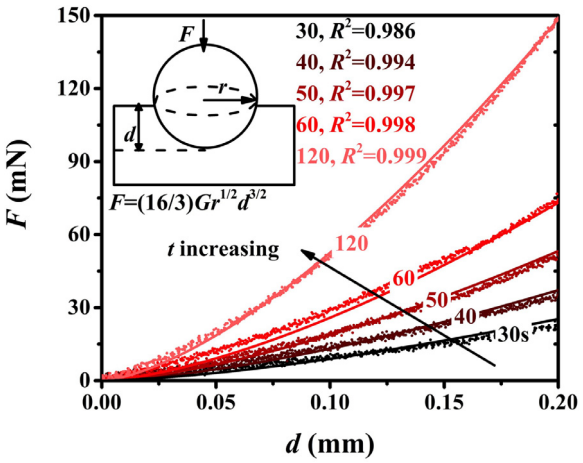

Fig. 4. Schematic of indentation measurements and representative data for hydrogels irradiated for prescribed time intervals. Indentation stiffness increased with increasing irradiation time, as represented by lines (Eq. (3)) and dots (experiment) of fading color (increasingly red in the online version). Lines represent fitting of Eq. (3) to obtain the shear modulus (G) of each sample. For this figure, the initial conditions for the sample were $[EY]_0 = 10\ \mu M$, $[TEOA]_0 = 100$ mM, and $[PEGDA]_0 = 20\%$. The illumination intensity was $I_0 = 50$ mW cm^{-2}.

3.4. Quantification of the gel point and shear modulus

2 mL of the polymer precursor poured into a 35 mm petri dish to form a hydrogel approximately 2 mm in height was subsequently irradiated using a LED (50 mW cm^{-2}) and tested on a MCR 302 rheometer (Anton-Paar, Graz, Austria) every 5 s over the course of illumination. Tests were performed at a 0.1% strain, 0.5 Hz frequency, and 0.1 N normal force. The gel point was defined as the point where the storage modulus (G') reached just above the loss modulus (G'') (Hao and Lin, 2014). The associated results are shown in Fig. B2.

Shear moduli were estimated on specimens identical to those above except irradiated for 30–120 s. Static indentation tests were performed on each crosslinked sample using a Bose Electroforce Biomaterial Test Instrument (Bose, MN, USA). A steel sphere 10 mm in diameter was used to compress the sample while force versus displacement were recorded at 10 Hz. The shear moduli (G) were calculated by Hertz indentation theory as follows (Hu et al., 2010):

$$F = (16/3)Gr^{1/2}d^{3/2} \tag{50}$$

where F is the force on the indenter, d is the indenter displacement, and r is the spheroid indenter radius. Stress-strain curves in the range of 0–0.1 strain were used to calculate the shear moduli. The measurement scheme and representative indentation curves of the samples at different irradiation times are shown in Fig. 4.

4. Discussion

4.1. Theoretical validation of photobleaching dependent photopolymerization kinetics

The photobleaching model (Eq. (2)) predicted the time evolution of photobleaching (X_{EY}) as measured by UV–Vis spectrometry (Fig. 5a–d, $R^2 = 0.854$–0.999). A single parameter, the photobleaching constant (k_{pb}), was obtained by fitting the experimental data. The relationships between kpb and $[EY]_0$ as well as I_0 and $[TEOA]_0$, described by Eq. (5), were also validated experimentally: kpb was unaffected by $[EY]_0$ (Fig. 5e), was proportional to I0 (Fig. 5f), and exhibited a sigmoidal functional relationship with the logarithm of $[TEOA]_0$ (Fig. 5g). The model predicted that [PEGDA]0 would not affect kpb, which agreed with experimental data, but only for $[PEGDA]_0 \leq 80\%$ (Fig. 5h). However, over the range $80\% \leq [PEGDA]_0 \leq 100\%$, kpb sharply decreased by an order of magnitude compared to the predicted value. This phenomenon can be attributed to the increasing viscosity of the precursors with increasing $[PEGDA]_0$. The increasing viscosity may decrease the diffusion rates of the chemical species, limiting the overall reaction kinetics.

The photopolymerization model (Eq. (19)), which incorporated the photobleaching process, predicted the time evolution of X_{CC} under different reaction conditions as measured via FTIR spectrometry (Fig. 6a–d, $R^2 = 0.918$–0.998). The beginning initiation rate (R_{i0}) was obtained for each reaction condition and the functional relationships between R_{i0} and $[EY]_0$, I_0, $[TEOA]_0$, and $[PEGDA]_0$ are shown in Fig. 6e–h, respectively. The model predictions were included in these graphs for comparison. As shown in Fig. 6f and g, R_{i0} increasing with increasing I_0 and $[TEOA]_0$ in both experimental data and model predictions. A slight deviation between the experimental data and modeling results at low I_0 or $[TEOA]_0$ was observed and could be attributed to the unconsidered oxygen-inhibiting effect (Dendukuri et al., 2008; Iedema et al., 2018). The predicted linear relationship by Eq. (16) between R_{i0} and varying $[EY]_0$ was only validated for $[EY]_0 \leq 10\ \mu M$ (dotted line in Fig. 6e).

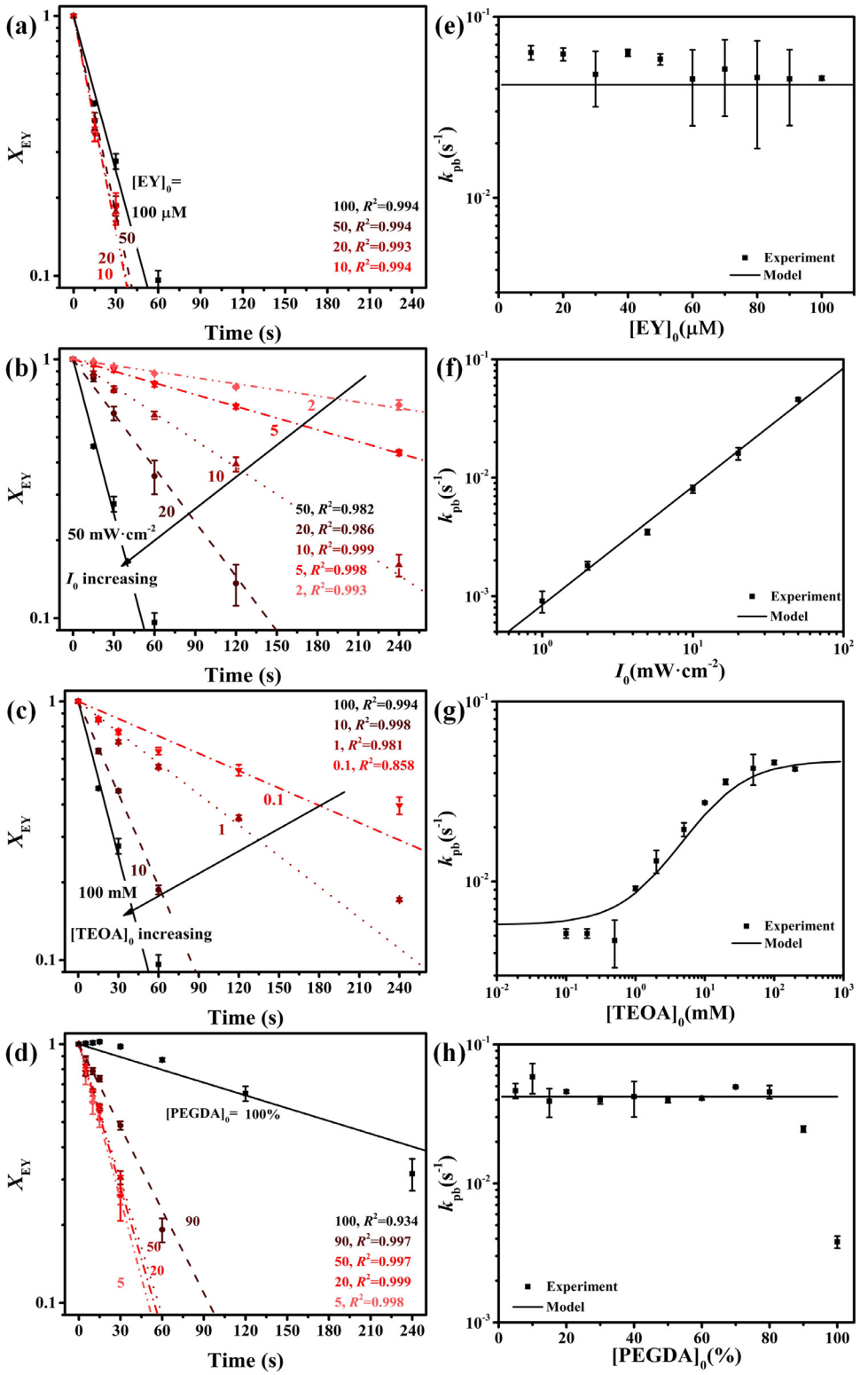

Fig. 5. The eosin Y conversion processes in an optically uniform film. Time evolution of the fractional concentration of eosin Y in the irradiated sample with four varying input parameters. (a) $[EY]_0$ (I_0 = 50 mW cm^{-2}, $[TEOA]_0$ = 100 mM, $[PEGDA]_0$ = 20%), (b) I_0 ($[EY]_0$ = 10 μM, $[TEOA]_0$ = 100 mM, $[PEGDA]_0$ = 20%), (c) $[TEOA]_0$ ($[EY]_0$ = 10 μM, I_0 = 50 mW cm^{-2}, $[PEGDA]_0$ = 20%), and (d) $[PEGDA]_0$ ($[EY]_0$ = 10 μM, I_0 = 50 mW cm^{-2}, $[TEOA]_0$ = 100 mM). The symbols are experimental data and lines are the fitting. The different colors indicate samples with different initial conditions. The photobleaching kinetic constant (k_{pb}) obtained by fitting as functions of $[EY]_0$, I_0, $[TEOA]_0$, $[PEGDA]_0$ are provided in the symbols in (e), (f), (g), and (h) respectively, and the lines in these figures were generated from our model.

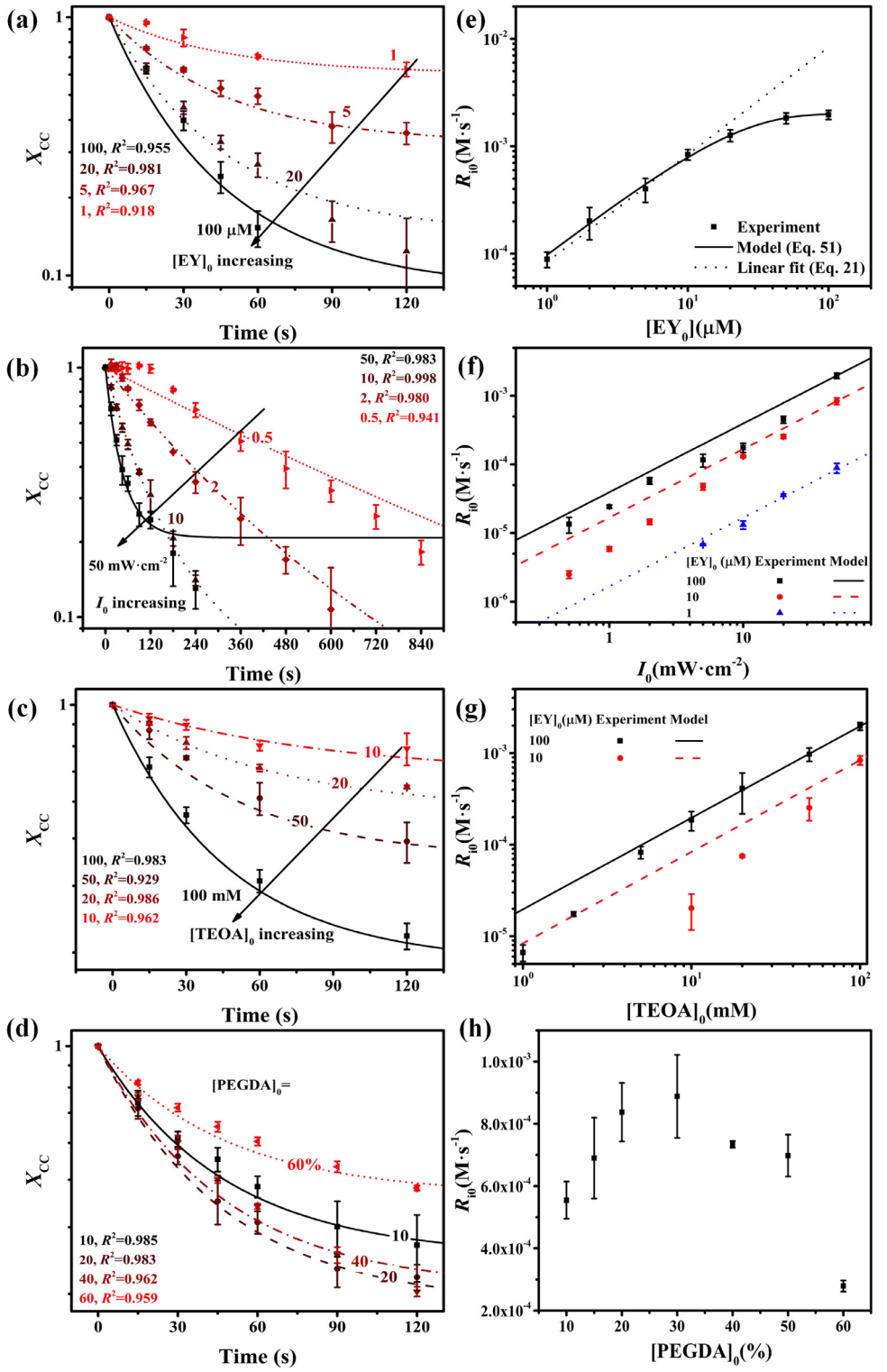

Fig. 6. Acrylate conversion in an optically uniform film. Time evolution of the fractional concentration of acrylates (X_{CC}) in an irradiated sample at different (a) initial eosin Y concentrations (other input parameters fixed at I_0 = 50 mW cm^{-2}, [TEOA]$_0$ = 100 mM, [PEGDA]$_0$ = 20%), (b) light intensities (other input parameters fixed at [EY]$_0$ = 10 μM, [TEOA]$_0$ = 100 mM, [PEGDA]$_0$ = 20%), (c) initial TEOA concentrations (other input parameters fixed at [EY]$_0$ = 10 μM, I_0 = 50 mW cm^{-2}, [PEGDA]$_0$ = 20%), and (d) initial PEGDA concentrations (other input parameters fixed at [EY]$_0$ = 10 μM, I_0 = 50 mW cm^{-2}, [TEOA]$_0$ = 100 mM). The symbols are experimental data and lines are the fitting. The different colors indicate samples with different initial conditions. The beginning initiation rates (R_{i0}) obtained by fitting are shown in symbols in (e), (f), (g), and (h), and the lines in these figures are the simulation results provided by the newly developed model.

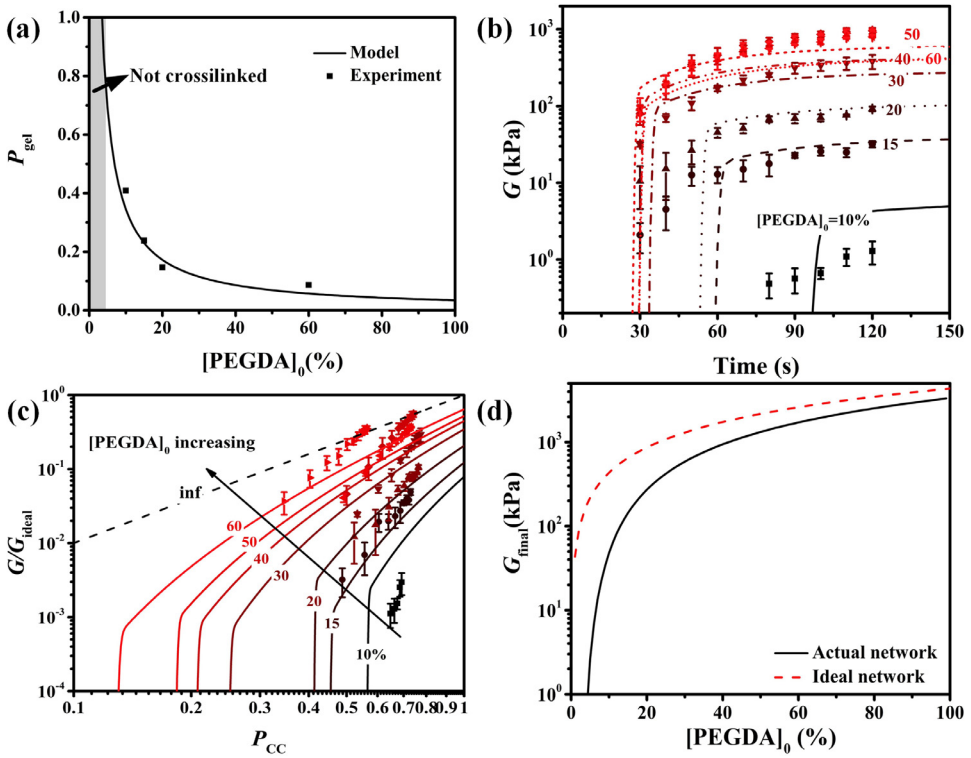

Fig. 7. Network analysis of the eosin Y-initiated PEGDA hydrogels. (a) The gel point (P_{gel}) of the hydrogels with different initial PEGDA concentrations ([PEGDA]$_0$). The symbols are experimental results and the line is the prediction provided by the modified recursive model. The gray region is the range of [PEGDA]$_0$ where the gel could not be crosslinked even when the acrylates were exhausted. (b) Time evolution of the shear moduli (G) under different [PEGDA]$_0$. The symbols are experimental results and lines are the prediction provided by the modified recursive model. The different colors indicate samples with [PEGDA]$_0$. (c) The DoC of acrylate (P_{CC})-dependent shear modulus ratios between the actual networks (G) and ideal networks (G_{ideal}) under different [PEGDA]$_0$. The symbols were calculated from the experimental results and lines are the predictions of the modified recursive model. The different colors indicate samples with [PEGDA]$_0$. The dashed line predicts the G/G_{ideal} as [PEGDA]$_0$ approached infinity, where loop formation processes are prevented. (d) The final shear moduli (G_{final}) of the actual and ideal networks and at different [PEGDA]$_0$. All results were obtained at [EY]$_0$ = 10 μM, [TEOA]$_0$ = 100 mM, and I_0 = 50 mW cm^{-2}.

With increasing [EY]$_0$, R_{i0} approached a constant value. To depict the R_{i0}-[EY]$_0$ profile at a defined [PEGDA]$_0$, Eq. (21) can be replaced by the following equation:

$$R_{i0} = \gamma/\omega \cdot (1 - \exp(-\omega[EY]_0))[TEOA]_0 I_0 \tag{51}$$

where ω is a fitting constant that is independent of [EY]$_0$, I_0, and [TEOA]$_0$. This modified relationship (the solid line in Fig. 6e) fit the experimental data. A parabolic relationship between R_{i0} and [PEGDA]$_0$ was observed (Fig. 6h), but this was not predicted by the model. When [PEGDA]$_0$ ranged from 15 to 50%, the time evolution of X_{CC} (Fig. 6d) and R_{i0} values (Fig. 6h, 6.9–8.9·10^{-4} M s^{-1}) were similar, while the consumption of acrylates significantly slowed when [PEGDA]$_0$ was over 60% (R_{i0} = 2.8·10^{-4} M s^{-1}).

4.2. Validation of gel point and mechanical property predictions

The experimentally obtained time of gelation (Fig. B2) was used to calculate the DoC of acrylates at the gel point (P_{gel}) using Eq. (26). The experimentally measured [PEGDA]$_0$-P_{gel} curve (dots in Fig. 7a) revealed that the gel point shifted to smaller values with increasing polymer concentration ([PEGDA]$_0$), which is common in polymer networks and attributed to loop formation (Wang et al., 2017b). This trend was accurately captured by the developed model (the line in Fig. 7a). Consistent with model predictions, experimental results revelaed that the gel was not crosslinked when [PEGDA]$_0$ was ≤5%, even when the acrylates were exhausted.

To validate predictions of mechanical properties, indentation tests were performed on photopolymerized hydrogels prepared using different [PEGDA]$_0$ and different curing times under a fixed I_0, [EY]$_0$, and [TEOA]$_0$. The shear moduli of the prepared hydrogels were calculated from the stress-strain curves obtained by the indentation experiments (Fig. 7b). With increasing curing time, the shear moduli of all samples increased, while the stiffness growth was slower and reached a steady state after 120 s. As [PEGDA]$_0$ increased from 10% to 40%, the final shear moduli increased from approximately 1.2

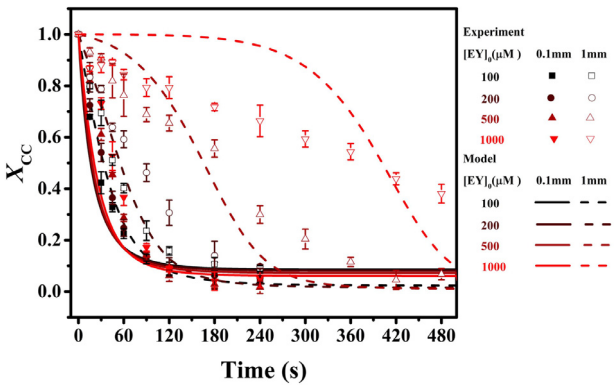

Fig. 8. Time evolution of acrylate conversion under different initial concentrations of eosin Y and thickness. The symbols are experimental data and lines are modeling results. The different colors indicate samples with $[EY]_0$. The solid symbol and lines indicate the sample with 0.1 mm thickness, while hollow symbols and dashed lines indicate the samples with 1 mm thickness. The other input parameters were fixed at I_0 = 50 mW cm^{-2}, $[PEGDA]_0$ = 20%, $[TEOA]_0$ = 100 mM.

to 960 kPa. Upon further increasing $[PEGDA]_0$ from 40% to 60%, the final shear moduli slightly decreased due to slower polymerization kinetics at high $[PEGDA]_0$. Model predictions showed good agreement with these experimental results.

We explored the maximum shear moduli that can be achieved for hydrogels with different $[PEGDA]_0$. P_{CC} was calculated at different curing times for each sample using the model. The final P_{CC} increased from 0.69 to 0.77 as the $[PEGDA]_0$ increased from 10% to 30%. However, upon further increasing $[PEGDA]_0$ to 60%, P_{CC} decreased to 0.56. The relationships between the relative shear moduli (G/G_{ideal}) and P_{CC} at different $[PEGDA]_0$ revealed that increasing conversion of acrylate stiffened the hydrogels at arbitrary fixed polymer concentrations (*i.e.* $[PEGDA]_0$): with increasing $[PEGDA]_0$, the shear modulus of the fully crosslinked hydrogel (P_{CC} = 1) approached that of the ideal network ($G_{final}/G_{ideal}\rightarrow 1$) due to the reduced probability of loop formation (Fig. 7c). As $[PEGDA]_0$ approaches 100%, the model predicted the maximum shear modulus of the actual photopolymerized and ideal networks of PEGDA (Mw = 575) of 3.3 and 4.3 MPa, respectively (Fig. 7d).

4.3. Prediction of frontal photopolymerization

We applied the model to design a graded hydrogel using FPP. Model predictions were validated by measuring PCC at the bottom of hydrogels with varying initiator concentrations and thicknesses by FTIR spectrometry (dots in Fig. 8). The experimental data showed that the time evolution of PCC was similar in the 0.1 mm film when $[EY]_0$ changed from 100 to 1000 μM, in accordance with the conclusions provided in Section 4.1. As the film thickness was increased to 1 mm, the time evolution processes of PCC showed differences in samples with different $[EY]_0$ due to differing absorption coefficients. At low [EY]0 (100 μM), the 1 mm film exhibited an approximately uniform crosslinking, resulting in a similar time-PCC profile as that of the 0.1 mm film. At high $[EY]_0$ (1000 μM), the 1 mm film strongly slowed acrylate conversion, in contrast to the 0.1 mm film. These phenomena were well captured by the developed model (lines in Fig. 8). To fit the experimental data, the molar absorption coefficient of eosin Y was set to 0.015 μM•mm^{-1} and the constant absorption coefficient of PEGDA hydrogels to 0.5 mm^{-1}, both of which are slightly larger than the peak values (0.009 μM mm^{-1}, 0.2 mm^{-1}) provided by the UV–Vis spectra (see Section 3.2). These results indicate that the developed model provides a reasonable prediction for FPP.

The model was also used to analyze the conversion profiles of eosin Y and acrylates in FPP. As described in the Introduction, Cabral's coarse-grained model provides a reasonable analysis of FPP. However, Cabral's coarse-grained model does not consider the concentration changes of initiators, which can affect the absorption coefficient and chemical kinetics simultaneously. The model developed herein considers the variance of multiple chemical species (*i.e.* acrylates, eosin Y), which provides a more detailed analysis and predictions for FPP. In a typical simulation of FPP in a hydrogel with a fixed composition ($[EY]_0$ = 10 μM, $[TEOA]_0$ = 100 mM, $[PEGDA]_0$ = 20%, I_0 = 50 mW cm^{-2}), distributions of P_{CC} and PEY varied with curing time and sample depth (Fig. 9a and b). The DoC at the positions (z_{CC0}, z_{EY0}), starting points (z_{CC1}, z_{EY1}), and end points (z_{CC2}, z_{EY2}) of the interface approached constant values ($P_{CC0,\,final}$ = 0.63, $P_{CC1,\,final}$ = 0.2, $P_{CC2,\,final}$ = 0.92, $P_{EY0,\,final}$ = 0.61, $P_{EY1,\,final}$ = 0.19, $P_{EY2,\,final}$ = 0.92) with progressing time. After 3000 s of light irradiation, the consumption of acrylate and eosin Y were not synchronous and the conversion interface of acrylate propagated more quickly than that of eosin Y in the z axis (Fig. 9c). The interfacial positions of acrylate and eosin Y both grew logarithmically with time, with the slope of acrylate significantly larger than that of eosin Y. Over time, the interfacial width of acrylate finally approached 7.51 mm, nearly twice that of eosin Y (4.11 mm) (Fig. 9d). The acrylate conversion profile and stiffness gradient were both time-invariant after sufficient irradiance dosing (after 960 s, Fig. 9e and f) as predicted by Cabral (Vitale et al., 2015a). It should be noted that the reverse stiffness gradient on the surface of the sample was caused by photobleaching.

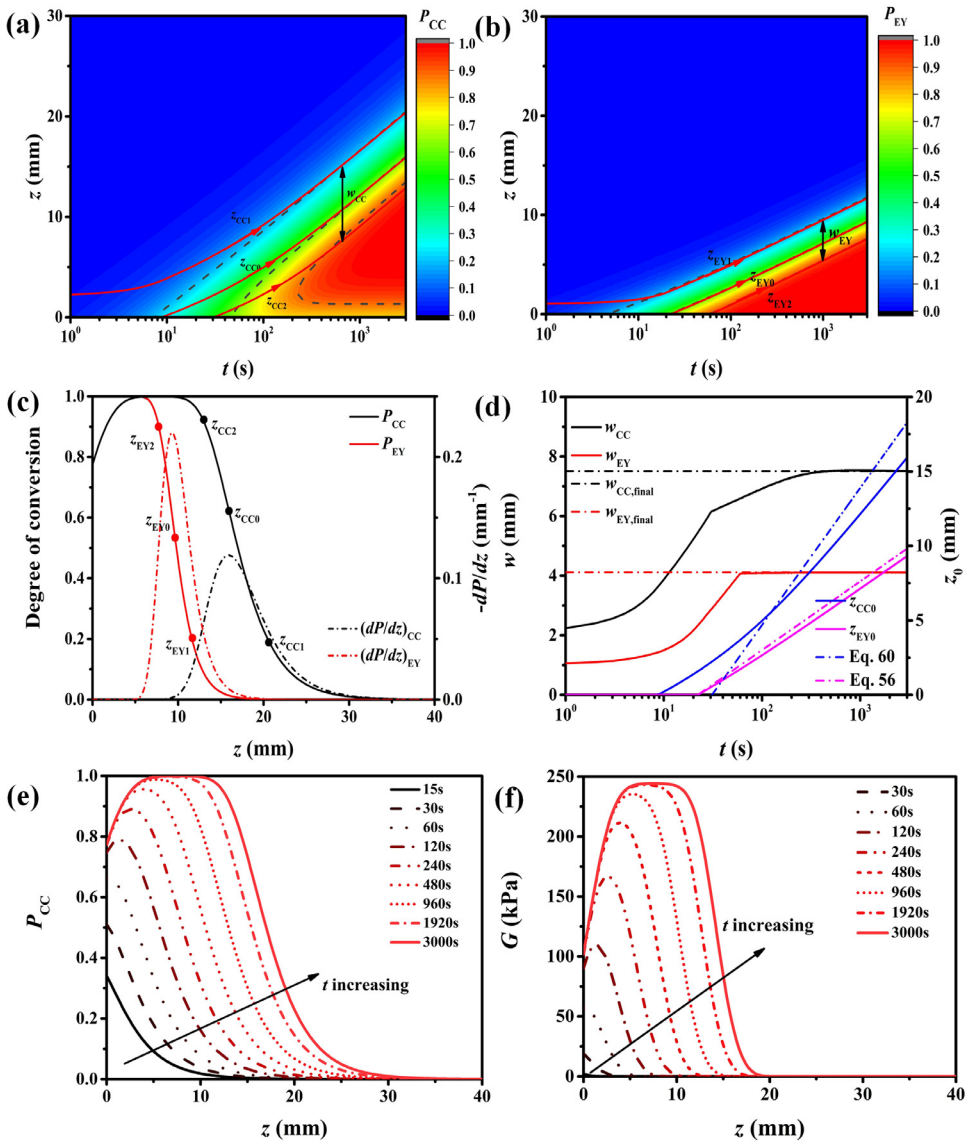

Fig. 9. Simulation of the spatiotemporally dependent degree of conversion and mechanical properties during frontal photopolymerization. (a) Contour plot of the DoC of acrylate (P_{CC}) varying with curing time (t) and sample depth (z). (b) Contour plot of the DoC of eosin Y (P_{EY}) varying with curing time (t) and sample depth (z). The red lines with arrows in (a, b) show the interfacial positions (z_{CC0}, z_{EY0}), beginning points (z_{CC1}, z_{EY1}), and end points (z_{CC2}, z_{EY2}) varying with time. The black lines with double arrows show the widths (w_{CC}, w_{EY}) of the interface. (c) Comparison of the conversion profiles of acrylate and eosin Y after curing for 3000 s. The interfacial positions (z_{CC0}, z_{EY0}), beginning points (z_{CC1}, z_{EY1}), and end points (z_{CC2}, z_{EY2}) were determined according to maximum and half maximum values of the DoC derivatives dP_{CC}/dz and dP_{EY}/dz. (d) Time evolution of the interface widths (w_{CC}, w_{EY}) and interfacial positions (z_{CC0}, z_{EY0}) on the eosin Y and acrylate conversion profiles. The red and black dashed lines represent the final interface widths of acrylate and eosin Y, respectively. The blue and magenta dashed lines represent the interfacial positions of acrylate and eosin Y, as predicted by Eqs. (60) and (56), respectively. (e) Dependence of the acrylate conversion profile along the sample depth (z) on curing time (t). The different colors and styles of lines indicate samples prepared with different irradiation times. (f) Dependence of the stiffness gradient along the sample depth (z) on curing time (t). The different colors and styles of lines indicate samples prepared with different irradiation times. All plots were calculated at $[EY]_0 = 10\ \mu M$, $[TEOA]_0 = 100$ mM $[PEGDA]_0 = 20\%$, $I_0 = 50$ mW cm^{-2}.

To examine the effects of the initial concentration of photo-initiators on the FPP kinetics, the conversion of acrylate and eosin Y as well as changes in shear modulus with $[EY]_0$ ranging from 1 to 1000 μM were simulated (Fig. 10). The interfacial positions (z_{CC0}, z_{EY0}) evolved over time at a rate that decreased and converged to the same value with increasing $[EY]_0$ (Fig. 10a). When $[EY]_0 \leq 10\ \mu M$, the effects of $[EY]_0$ on the variances of both z_{CC0} and z_{EY0} were small, indicating that the sample was nearly photo-invariant. The final widths of the interfaces ($w_{CC,\ final}$ and $w_{EY,\ final}$) also decreased with increasing $[EY]_0$, with higher $[EY]_0$ resulting in a sharper conversion slope (Fig. 10b). Cabral showed that the interface width of the conversion profile (w) exhibits a reciprocal relationship with the average absorption coefficient ($\bar{\mu}$) as $w = e/\bar{\mu}$ (Hennessy et al., 2015a). Therefore, e/μ_0 was plotted as a function of $[EY]_0$, which is very similar to the $w_{EY,\ final}$-$[EY]_0$ curve. The acrylate

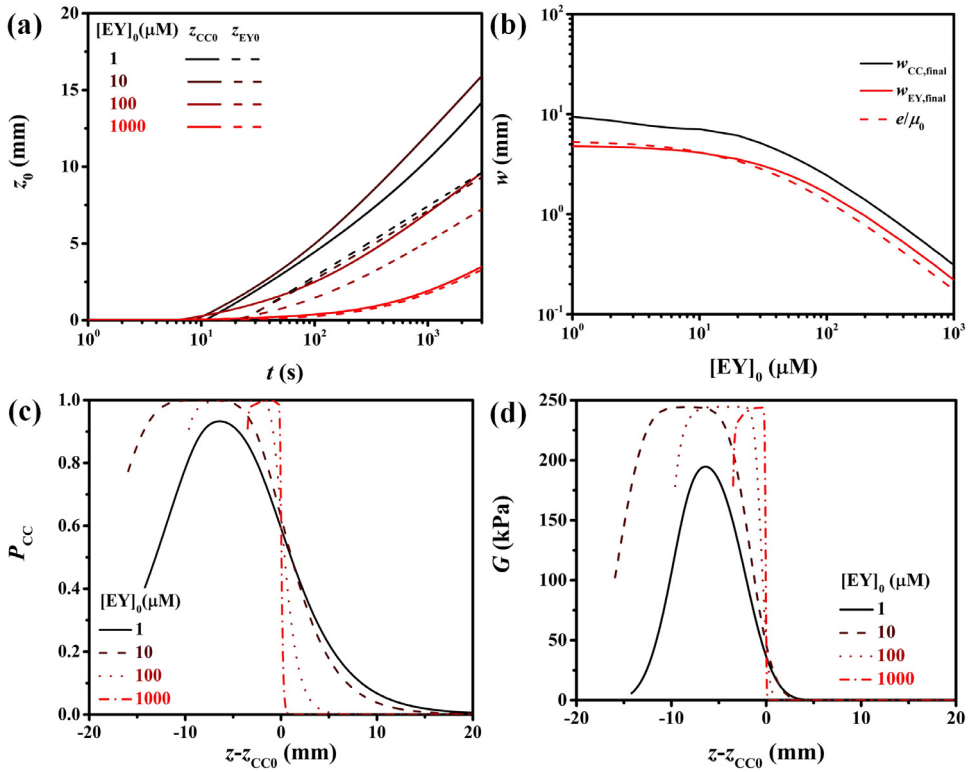

Fig. 10. Role of the initial eosin Y concentration on the conversion profile and stiffness gradient during frontal photopolymerization. (a) The effects of $[EY]_0$ on the time evolution profiles of the interfacial positions (z_{CC0}, z_{EY0}) on the acrylate (solid lines) and eosin Y (dashed lines) conversion profiles. (b) The effects of $[EY]_0$ on the final widths ($w_{CC,\,final}$ and $w_{EY,\,final}$). The dashed line shows the prediction of the interface width and conversion profiles from Cabral's coarse-grained model. (c) The effect of $[EY]_0$ on the acrylate conversion profiles. The curing time was set to 3000 s. The different colors and styles of lines indicate samples prepared with different $[EY]_0$. (d) The effect of $[EY]_0$ on the stiffness gradients (curing time of 3000 s). The different colors and styles of lines indicate samples prepared with different $[EY]_0$. All data were calculated at $[TEOA]_0$ = 100 mM, $[PEGDA]_0$ = 20%, I_0 = 50 mW cm^2.

conversion profile and the slope and strength of the stiffness gradient all steepened with increasing $[EY]_0$ (Fig. 10c and d): at $[EY]_0$ from 1 to 1000 mM, the average strength of the stiffness gradient (stiffness ranging from 1 to 190 kPa) increased from 21 to 792 kPa/mm.

Many of these model predictions were also observed in Cabral's coarse-grained model, including the observations that (i) interfacial positions increase logarithmically over time, (ii) the conversion profile shape and stiffness gradient at the interface become time-invariant after sufficient curing time, and (iii) the final widths of the interface are nearly reciprocal to the absorption coefficient. However, our model also predicted some new phenomena that have not been reported previously and that are beyond the scope of the Cabral model. These include observations that (i) the conversion profiles of the initiator and polymer were not synchronous, and (ii) the initiator concentration changed the shape of the conversion profile and strength of the stiffness gradient.

To further explore these new phenomena, the model was simplified to yield equations for eosin Y and acrylate conversion.

(1) Conversion profile of eosin Y

From Eq. (2), the spatiotemporally dependent conversion of eosin Y was described as:

$$\frac{dP_{EY}(z,t)}{dt} = -k_{pb}(1 - P_{EY}(z,t)) \tag{52}$$

From Eq. (41), the spatiotemporally dependent absorption coefficient was re-expressed as:

$$\mu(z,t) = -\mu_0(1 - P_{EY}(z,t)) + \mu_{const}P_{EY}(z,t) \tag{53}$$

From the generalized Beer-Lambert law, the distribution of light intensity (I) in the sample was described as:

$$\frac{dI(z,t)}{dz} = -\mu(z,t)I(z,t) \tag{54}$$

Because $k_{pb} \propto I(z,t)$, Eqs. (52)–(54) exhibit exactly the same form as Cabral's governing equations for the conversion fraction in FPP (Cabral and Douglas, 2005; Cabral et al., 2004; Warren et al., 2005). Thus, some conclusions obtained from Cabral's equations were suitable for conversion profile of eosin Y in the model developed herein.

For the photoinvariant case (when $[EY]_0$ is sufficiently low, $\mu = \mu_0 = \mu_{Const}$), Eqs. (52)–(54) showed that the spatiotemporally dependent P_{EY} is:

$$P_{EY}(z,t) = 1 - \exp\left(-k_{pb} \exp\left(-\mu_{const} z\right) t\right) \tag{55}$$

Thus, the interfacial positions on the conversion profile of eosin Y (z_{EY0}) grew logarithmically as:

$$\begin{cases} z_{EY0} = h_{EY} \ln\left(\frac{t}{T_{EY}}\right) \\ h_{EY} = \frac{1}{\mu_{const}}, T_{EY} = -\ln\left(1 - P_{EY0}\right)/k_{pb} \end{cases} \tag{56}$$

Eq. (56) indicates that in photoinvariant case, z_{EY0} exhibited a linear relationship with the logarithm of time after an induction time T_{EY}, and the slope (h_{EY}) is the reciprocal of μ_{Const}. In Fig. 9d, Eq. (56) predicted the dependence of z_{EY0} on time similarly to the experimental data and previous model, indicating that it is suitable for estimating the interfacial positions of the eosin Y conversion profile when $[EY]_0$ is $\leq$10 μM.

(2) Conversion profile of acrylate

In contrast, the conversion of acrylate is not synchronous with eosin Y. To simplify the deviation, we first reformed Eq. (19) by Taylor expansion as follows:

$$\begin{aligned} X_{CC} = \frac{[CC]}{[CC]_0} &= \exp\left(-b + b\left(1 - \frac{k_{pb}t}{2} + \frac{1}{2!}\left(\frac{k_{pb}t}{2}\right)^2 \cdots\right)\right) \\ &= \exp\left(-b\left(\frac{k_{pb}t}{2} + \frac{1}{2!}\left(\frac{k_{pb}t}{2}\right)^2 \cdots\right)\right) \end{aligned} \tag{57}$$

When $k_{pb}t<1$, the high order terms are negligible, and the conversion process was simplified as an exponential function:

$$\frac{dP_{cc}(z,t)}{dt} = -\frac{dX_{cc}(z,t)}{dt} = \frac{bk_{pb}}{2}\left(1 - P_{cc}(z,t)\right) = K\left(1 - P_{cc}(z,t)\right) \tag{58}$$

where K is the acrylate conversion constant, and $K = k_p\sqrt{R_i/k_t} \propto I(z,t)^{0.5}$. Because K is dependent on the concentration of eosin Y, the value of K varied with time and space.

To further simplify Eq. (58), the concentration of eosin Y was set as invariant ($[EY]_0$) and the surface acrylate conversion constant was set as $K_0 = k_p\sqrt{R_{i0}/k_t}$. In the photoinvariant case,

$$P_{CC}(z,t) = 1 - \exp\left(-K_0 \exp\left(-0.5\mu_{const} z\right) t\right) \tag{59}$$

Thus, the interfacial positions on conversion profile of acrylate (z_{CC0}) grew logarithmically as follows:

$$\begin{cases} z_{CC0} = h_{CC} \ln\left(\frac{t}{T_{CC}}\right) \\ h_{EY} = \frac{2}{\mu_{const}}, T_{CC} = -\ln\left(1 - P_{CC0}\right)/k_{pb} \end{cases} \tag{60}$$

This equation indicates that, similar to eosin Y, z_{CC0} also exhibited a logarithmic relationship with time after the induction time, T_{CC}, but the slope (h_{CC}) was twice that of eosin Y (h_{EY}). From Eq. (58), when acrylate conversion was completed within $t \in [0,\ 1/k_{pb})$, the effect of photobleaching could be omitted. The predicted results from Eq. (60) followed the trend of the simulated z_{CC0}-t curve (Fig. 9d). Although Cabral's coarse-grained model provides a reasonable fitting to experimental results, identifying the meaning of the fitting parameters is beyond its scope. The newly developed model provides a predicted distribution of eosin Y and acrylate and a clearer link between the molecular conversion processes and changes in the optical and mechanical properties of photopolymerized hydrogels.

5. Conclusions

A multiscale model of chemical kinetics and network mechanics was developed to describe the spatiotemporal evolution of optical and mechanical properties during photopolymerization, and was validated against eosin Y-initiated di-acrylate hydrogels. The model is the first of its kind to include predictive frameworks for photobleaching and loop formation. Results showed important effects of these parameters on the ways that the parameters initial conditions $[EY]_0$, $[TEOA]_0$, and $[PEGDA]_0$ and irradiation intensity I_0 affect the chemical kinetics and mechanical properties of the resulting hydrogels.

The model had only two fitting parameters: the photobleaching kinetic rate constant (k_{pb}) and beginning initiation rate (R_{i0}). The model correctly predicted that k_{pb} is invariant with respect to $[EY]_0$, varies as a sigmoidal-like function of the logarithm of $[TEOA]_0$, is invariant of $[PEGDA]_0$ over a limited range (0–80%), and increases linearly with I_0. The model also predicted correctly that R_{i0} increases linearly with $[EY]_0$ within a limited range (0–10 μM) increased linearly with $[TEOA]_0$ and I_0, and exhibited a parabolic relationship with $[PEGDA]_0$.

The modified recursive model, including effects of loop formation, predicted how the DoC of acrylate and the variation of $[PEGDA]_0$ affected gelation and shear moduli. The model predicted that the network shear modulus could reach 3/4 of the ideal network modulus as acrylates are exhausted and $[PEGDA]_0$ reaches 100%.

The model has broad utility for designing hydrogels with defined spatial gradients of material properties. This was demonstrated by designing and fabricating a graded hydrogel via an FPP process. By harnessing the way that propagation of the acrylate conversion profile is slower than that of eosin Y, well-defined, tunable gradients were possible, suggesting a broadly applicable tool for defining hydrogels for use across a broad range of applications.

Declaration of Competing Interest

The authors declare the following financial interests/personal relationships which may be considered as potential competing interests: Guy Genin holds equity in Caeli Vascular, LLC, and holds patents on adhesive repairs of orthopedic injuries, including hydrogel adhesives.

Acknowledgements

This work was supported by the National Natural Science Foundation of China (11772253, 11532009), the Shaanxi Province Youth Talent Support Program, the Young Talent Support Plan of Xi'an Jiaotong University, the National Institutes of Health (U01EB016422), and the NSF Science and Technology Center for Engineering Mechanobiology (CMMI 1548571).

Appendix A

Table A1
Reactions modeled.

Initiation	
$EY_0 \leftrightarrow EY^{3*}$ k_1, k_2	(R1)
$EY^{3*} + TEOA \rightarrow EY^{-} + TEOA^{\cdot}$ k_3	(R2)
$EY^{-} \rightarrow EY_0$ k_4	(R3)
$EY^{-} \rightarrow EYH_2$ k_5	(R4)
Propagation	
$TEOA^{\cdot} + CC \rightarrow CC^{\cdot}$ k_i	(R5)
$CC^{\cdot} + CC \rightarrow CC^{\cdot}$ k_p	(R6)
Termination	
$CC^{\cdot} + CC^{\cdot} \rightarrow P$ k_t	(R7)

Table A2
Parameters used in the developed model.

Notation	Variable	Value	Unit	Ref
T	Temperature	300	K	–
h	Planck's constant	$6.63 \cdot 10^{-34}$	J•s	(Svelto and Hanna, 1976)
ν	The peak frequency of emission spectrum of LED	$5.77 \cdot 10^{14}$	s^{-1}	(Zhu et al., 2018)
k_2	Relaxation rate of eosin Y triplet state	$4 \cdot 10^{5}$	s^{-1}	(Gorner, 2008)
k_4	Rate constant for eosin Y relaxation from anion radical state to ground state	$3 \cdot 10^{4}$	s^{-1}	(Gorner, 2008)
k_5	Rate constant for leuco-product generation by eosin Y anion radicals	175	s^{-1}	estimated [a]
σ	Absorption cross-section of eosin Y ground state	$6.2 \cdot 10^{-17}$	cm^2	(Penzkofer and Beidoun, 1993)
k_{et}	Electron transfer rate constant to SH	$3.45 \cdot 10^{7}$	$M^{-1}s^{-1}$	estimated [a]
k_{et0}	Electron transfer rate constant to other molecules	$5.58 \cdot 10^{4}$	s^{-1}	estimated [a]
k_i	Kinetic constant of initiating acrylate by TEOA•	0.3784	$M^{-1} \cdot s^{-1}$	(Lee et al., 2014)
k_{ct}	Kinetic constant of chain transfer of acrylate radical to TEOA	0.3825	$M^{-1} \cdot s^{-1}$	(Lee et al., 2014)
k_p	Kinetic constant of acrylate radical propagation	$4.94 \cdot 10^{3}$	$M^{-1} \cdot s^{-1}$	(Lee et al., 2014)
k_t	Kinetic constant of radical termination	$9.55 \cdot 10^{6}$	$M^{-1} \cdot s^{-1}$	(Lee et al., 2014)
γ	Fitting constant of initiation	20	$M^{-1}mJ^{-1}cm^2$	estimated [a]
ω	Fitting constant of initiation	$5 \cdot 10^{4}$	M^{-1}	estimated [a]
C_0	Critical initial PEGDA concentration for curing the precursor	3.45	%	estimated [a]
ε_{EY}	Molar absorption of eosin Y	0.015	$\mu M^{-1}mm^{-1}$	estimated [a]
μ_0	Constant absorbance of PEGDA hydrogels	0.5	mm^{-1}	estimated [a]

[a] Values estimated by fitting experimental data.

Appendix B

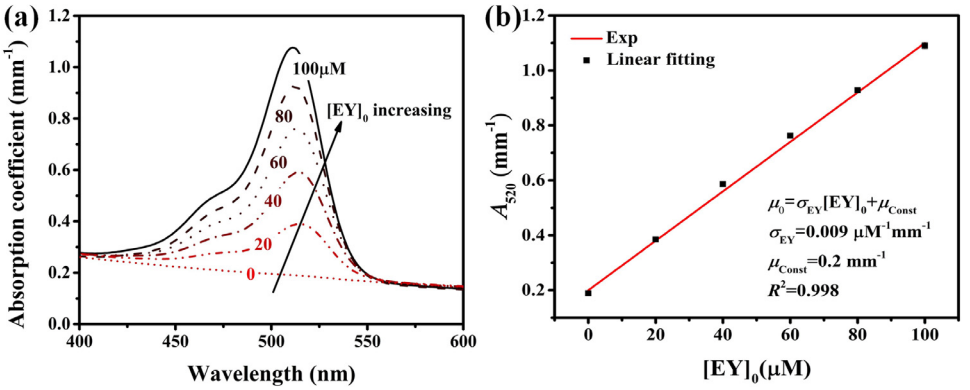

Fig. B1. Experimental quantification of the absorption coefficient of hydrogel precursor. (a) The dependence between the wavelength absorption coefficient (absorbance per unit thickness of sample) and $[EY]_0$. The different colors and styles of lines indicate precursors with different $[EY]_0$. (b) The linear dependence of absorption coefficient on 520 nm on $[EY]_0$. This measurement provided the absorbance value with accurate depth information.

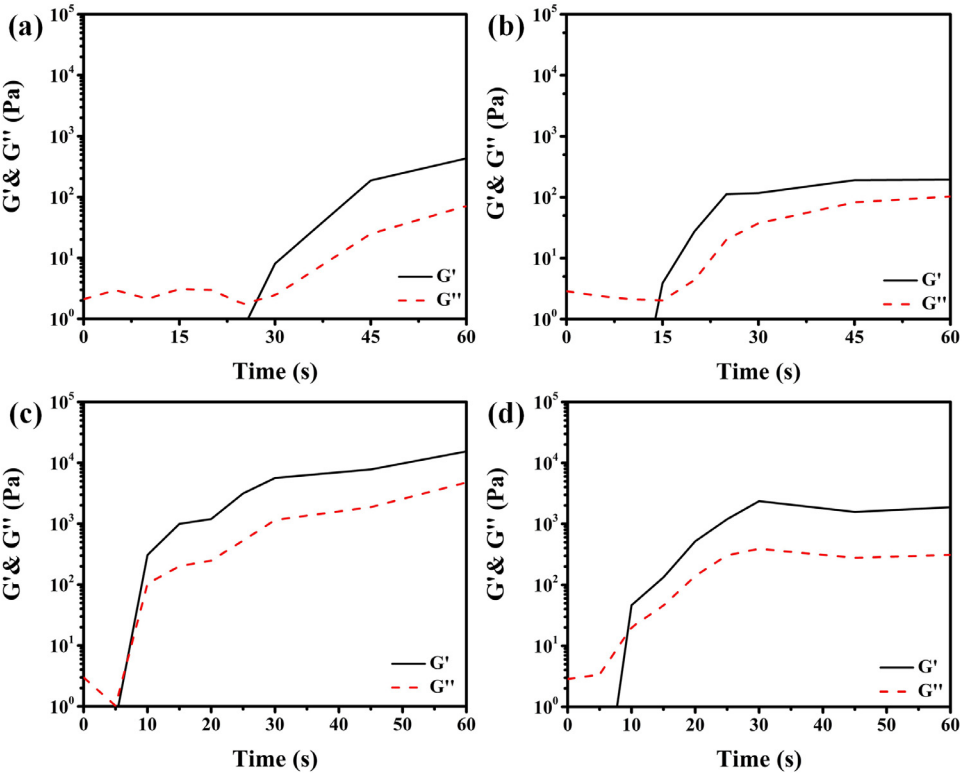

Fig. B2. Results of the rheological tests for measuring gel points. Gel points are the points when the storage modulus (G') is surpassed loss modulus (G''). The initial concentration of PEGDA in the sub-graphs are (a) $[PEGDA]_0$ = 10%, (b) $[PEGDA]_0$ = 15%, and (c) $[PEGDA]_0$ = 20%, $[PEGDA]_0$ = 60%, while the other reaction conditions were constant as $[EY]_0$ = 10 μM, $[TEOA]_0$ = 100 mM, and I_0 = 50 mW cm^{-2}.

References

Boonen, H.A.L., Koskamp, J.A., Theiss, W., Iedema, P.D., Willemse, R.X.E., 2017. Simultaneous Real-Time Analysis of Bulk and Bottom Cure of Ultraviolet-Curable Inks Using Fourier Transform Infrared Spectroscopy. Appl. Spectrosc. 71, 2699–2706.

Brown, T.E., Anseth, K.S., 2017. Spatiotemporal hydrogel biomaterials for regenerative medicine. Chem. Soc. Rev. 46, 6532–6552.

Cabral, J.T., Douglas, J.F., 2005. Propagating waves of network formation induced by light. Polymer (Guildf) 46, 4230–4241.

Cabral, J.T., Hudson, S.D., Harrison, C., Douglas, J.F., 2004. Frontal Photopolymerization for Microfluidic Applications. Langmuir 20, 10020–10029.

Corrigan, N., Yeow, J., Judzewitsch, P., Xu, J., Boyer, C.A.J.M., 2018. Seeing the light: advancing materials chemistry through photopolymerization. Angew. Chem. 131, 5224–5243.

Cramer, N.B., Davies, T., O'Brien, A.K., Bowman, C.N., 2003. Mechanism and modeling of a thiol−ene photopolymerization. Macromolecules 36, 4631–4636.

Dadashi-Silab, S., Doran, S., Yagci, Y., 2016. Photoinduced electron transfer reactions for macromolecular syntheses. Chem. Rev. 116, 10212–10275.

Dendukuri, D., Panda, P., Haghgooie, R., Kim, J.M., Hatton, T.A., Doyle, P.S., 2008. Modeling of oxygen-inhibited free radical photopolymerization in a PDMS microfluidic device. Macromolecules 41, 8547–8556.

Dutton, S., Stepto, R.F.T., Taylor, D.J.R., 1996. Monte-carlo modelling of the formation, structure and properties of polymer networks. Angew. Makromol. Chem. 240, 39–57.

Feng, X., Ma, Z., MacArthur, J.V., Giuffre, C.J., Bastawros, A.F., Hong, W., 2016. A highly stretchable double-network composite. Soft Matter 12, 8999–9006.

Flory, P.J., 1941. Molecular size distribution in three dimensional polymers. I. Gelation. J. Am. Chem. Soc. 63, 3083–3090.

Gao, X., Shi, Z., Kuśmierczyk, P., Liu, C., Yang, G., Sevostianov, I., Silberschmidt, V.V., 2016. Time-dependent rheological behaviour of bacterial cellulose hydrogel. Mat. Sci. Eng. C 58, 153–159.

Gorner, H., 2008. Oxygen uptake induced by electron transfer from donors to the triplet state of methylene blue and xanthene dyes in air-saturated aqueous solution. Photoch. Photobio. Sci. 7, 371–376.

Hao, Y., Lin, C.-C., 2014. Degradable thiol-acrylate hydrogels as tunable matrices for three-dimensional hepatic culture. J. Biomed. Mater. Res. A 102, 3813–3827.

Hennessy, M.G., Vitale, A., Cabral, J.T., Matar, O.K., 2015a. Role of heat generation and thermal diffusion during frontal photopolymerization. Phys. Rev. E 92, 022403.

Hennessy, M.G., Vitale, A., Matar, O.K., Cabral, J.T., 2015b. Controlling frontal photopolymerization with optical attenuation and mass diffusion. Phys. Rev. E 91, 062402.

Hennessy, M.G., Vitale, A., Matar, O.K., Cabral, J.T., 2017. Monomer diffusion into static and evolving polymer networks during frontal photopolymerisation. Soft Matter 13, 9199–9210.

Herculano, L.S., Malacarne, L.C., Zanuto, V.S., Lukasievicz, G.V.B., Capeloto, O.A., Astrath, N.G.C., 2013. Investigation of the photobleaching process of eosin Y in aqueous solution by thermal lens spectroscopy. J. Phys. Chem. B 117, 1932–1937.

Hu, Y., Zhao, X., Vlassak, J.J., Suo, Z., 2010. Using indentation to characterize the poroelasticity of gels. Appl. Phys. Lett. 96, 121904.

Iedema, P.D., Schamböck, V., Boonen, H., Koskamp, J., Schellekens, S., Willemse, R., 2018. Photocuring of di-acrylate. Chem. Eng. Sci. 176, 491–502.

Krishnan, D., Johnson, H.T., 2014. Light-induced deformation in a liquid crystal elastomer photonic crystal. J. Mech. Phys. Solids 62, 48–56.

Layani, M., Wang, X., Magdassi, S., 2018. Novel materials for 3D printing by photopolymerization. Adv. Mater. 30, 1706344.

Lee, C.-Y., Teymour, F., Camastral, H., Tirelli, N., Hubbell, J.A., Elbert, D.L., Papavasiliou, G., 2014. Characterization of the network structure of PEG diacrylate hydrogels formed in the presence of N-vinyl pyrrolidone. Macromol. React. Eng. 8, 314–328.

Lendlein, A., Jiang, H., Junger, O., Langer, R., 2005. Light-induced shape-memory polymers. Nature 434, 879–882.

Lin, T.-S., Wang, R., Johnson, J.A., Olsen, B.D., 2018. Topological structure of networks formed from symmetric four-arm precursors. Macromolecules 51, 1224–1231.

Long, K.N., Scott, T.F., Jerry Qi, H., Bowman, C.N., Dunn, M.L., 2009. Photomechanics of light-activated polymers. J. Mech. Phys. Solids 57, 1103–1121.

Ma, J., Mu, X., Bowman, C.N., Sun, Y., Dunn, M.L., Qi, H.J., Fang, D., 2014. A photoviscoplastic model for photoactivated covalent adaptive networks. J. Mech. Phys. Solids 70, 84–103.

Macosko, C.W., Miller, D.R., 1976. A new derivation of average molecular weights of nonlinear polymers. Macromolecules 9, 199–206.

Miller, D.R., Macosko, C.W., 1976. A new derivation of postgel properties of network polymers. Rubber Chem. Technol. 49, 1219–1231.

Nishi, K., Fujii, K., Chung, U.-i., Shibayama, M., Sakai, T., 2017. Experimental observation of two features unexpected from the classical theories of rubber elasticity. Phys. Rev. Lett. 119, 267801.

Penzkofer, A., Beidoun, A., 1993. Triplet-triplet absorption of eosin Y in methanol determined by nanosecond excimer laser excitation and picosecond light continuum probing. Chem. Phys. 177, 203–216.

Reddy, S.K., Okay, O., Bowman, C.N., 2006. Network development in mixed step-chain growth thiol− vinyl photopolymerizations. Macromolecules 39, 8832–8843.

Rolfes, H., Stepto, R.F.T., 1990. Network formation and properties: rate theory description of effects of ring formation on elastic shear modulus of RA2 + RB3 networks. Makromol. Chem. Macromol. Symp. 40, 61–79.

Ruskowitz, E.R., DeForest, C.A., 2018. Photoresponsive biomaterials for targeted drug delivery and 4D cell culture. Nat. Rev. Mater. 3, 17087.

Shih, H., Lin, C.-C., 2013. Visible-light-mediated thiol-ene hydrogelation using eosin-Y as the only photoinitiator. Macromol. Rapid Comm. 34, 269–273.

Svelto, O., Hanna, D.C., 1976. Principles of Lasers. Springer.

Vitale, A., Cabral, T.J., 2016. Frontal conversion and uniformity in 3d printing by photopolymerisation. Materials (Basel) 9, 760.

Vitale, A., Hennessy, M.G., Matar, O.K., Cabral, J.T., 2015a. Interfacial profile and propagation of frontal photopolymerization waves. Macromolecules 48, 198–205.

Vitale, A., Hennessy, M.G., Matar, O.K., Cabral, J.T., 2015b. A unified approach for patterning via frontal photopolymerization. Adv. Mater. 27, 6118–6124.

Wang, L., Li, Y., Huang, G., Zhang, X., Pingguan-Murphy, B., Gao, B., Lu, T.J., Xu, F., 2016a. Hydrogel-based methods for engineering cellular microenvironment with spatiotemporal gradients. Crit. Rev. Biotechnol. 36, 553–565.

Wang, R., Alexander-Katz, A., Johnson, J.A., Olsen, B.D., 2016b. Universal cyclic topology in polymer networks. Phys. Rev. Lett. 116, 188302.

Wang, R., Johnson, J.A., Olsen, B.D., 2017a. Odd–even effect of junction functionality on the topology and elasticity of polymer networks. Macromolecules 50, 2556–2564.

Wang, R., Lin, T.-S., Johnson, J.A., Olsen, B.D., 2017b. Kinetic Monte Carlo simulation for quantification of the gel point of polymer networks. ACS Macro Lett. 6, 1414–1419.

Wang, R., Sing, M.K., Avery, R.K., Souza, B.S., Kim, M., Olsen, B.D., 2016c. Classical challenges in the physical chemistry of polymer networks and the design of new materials. Acc. Chem. Res. 49, 2786–2795.

Warren, J.A., Cabral, J.T., Douglas, J.F., 2005. Solution of a field theory model of frontal photopolymerization. Phys. Rev. E 72, 021801.

Wu, J., Zhao, Z., Hamel, C.M., Mu, X., Kuang, X., Guo, Z., Qi, H.J., 2018. Evolution of material properties during free radical photopolymerization. J. Mech. Phys. Solids 112, 25–49.

Yao, H., Wang, J., Mi, S., 2018. Photo processing for biomedical hydrogels design and functionality: a review. Polymers (Basel) 10, 11.

Yuk, H., Lu, B., Zhao, X., 2019. Hydrogel bioelectronics. Chem. Soc. Rev 48, 1642–1667.

Zhong, M., Wang, R., Kawamoto, K., Olsen, B.D., Johnson, J.A., 2016. Quantifying the impact of molecular defects on polymer network elasticity. Science 353, 1264.

Zhou, H., Woo, J., Cok, A.M., Wang, M., Olsen, B.D., Johnson, J.A., 2012. Counting primary loops in polymer gels. P. Natl. Acad. Sci. USA 109, 19119–19124.
Zhu, H., Yang, X., Genin, G.M., Lu, T.J., Xu, F., Lin, M., 2018. The relationship between thiol-acrylate photopolymerization kinetics and hydrogel mechanics: an improved model incorporating photobleaching and thiol-Michael addition. J. Mech. Behav. Biomed. 88, 160–169.
Zou, W., Dong, J., Luo, Y., Zhao, Q., Xie, T., 2017. Dynamic covalent polymer networks: from old chemistry to modern day innovations. Adv. Mater. 29, 1606100.